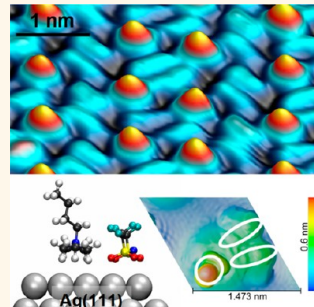


Toward the Microscopic Identification of Anions and Cations at the Ionic Liquid|Ag(111) Interface: A Combined Experimental and Theoretical Investigation

Florian Buchner,^{†,‡,§,⊥} Katrin Forster-Tonigold,^{†,§,⊥} Benedikt Uhl,^{†,‡} Dorothea Alwast,^{†,‡} Nadja Wagner,^{†,‡} Hanieh Farkhondeh,^{†,‡} Axel Groß,^{†,§} and R. Jürgen Behm^{†,‡,*,}

[†]Helmholtz Institute Ulm – Electrochemical Energy Storage, Albert-Einstein-Allee 11, D-89081 Ulm, Germany, [‡]Institute of Surface Chemistry and Catalysis, Ulm University, Albert-Einstein-Allee 47, D-89081 Ulm, Germany, and [§]Institute of Theoretical Chemistry, Ulm University, Albert-Einstein-Allee 11, D-89081 Ulm, Germany. [⊥]F. Buchner and K. Forster-Tonigold contributed equally.

ABSTRACT The interaction between an adsorbed 1-butyl-1-methylpyrrolidinium bis(trifluoromethylsulfonyl)imide, [BMP][TFSA], ionic liquid (IL) layer and a Ag(111) substrate, under ultrahigh-vacuum conditions, was investigated in a combined experimental and theoretical approach, by high-resolution scanning tunneling microscopy (STM), X-ray photoelectron spectroscopy (XPS), and dispersion-corrected density functional theory calculations (DFT-D). Most importantly, we succeeded in unambiguously identifying cations and anions in the adlayer by comparing experimental images with submolecular resolution and simulated STM images based on DFT calculations, and these findings are in perfect agreement with the 1:1 ratio of anions and cations adsorbed on the metal derived from XPS measurements. Different adlayer phases include a mobile 2D liquid phase at room temperature and two 2D solid phases at around 100 K, *i.e.*, a 2D glass phase with short-range order and some residual, but very limited mobility and a long-range ordered 2D crystalline phase. The mobility in the different adlayer phases, including melting of the 2D crystalline phase, was evaluated by dynamic STM imaging. The DFT-D calculations show that the interaction with the substrate is composed of mainly van der Waals and weak electrostatic (dipole–induced dipole) interactions and that upon adsorption most of the charge remains at the IL, leading to attractive electrostatic interactions between the adsorbed species.



KEYWORDS: ionic liquids · scanning tunneling microscopy · density functional theory · surface chemistry · self-assembly · molecule–molecule and molecule–substrate interactions

Ionic liquids (ILs), which are molten salts usually consisting of organic ions with a melting point below 100 °C,^{1,2} have attracted considerable interest in recent years because of their unusual physicochemical properties such as high ionic conductivity and electrochemical stability, very low vapor pressure, or low flammability. Due to the large variety of combinations of different anion–cation pairs, the properties of the ILs can be adjusted over a wide range, making them highly interesting molecular building blocks for both fundamental research and specific applications.^{1–4} One very interesting application is their use as solvent in electrochemical energy storage, where ionic liquids could replace standard solvents in

lithium ion and lithium air batteries.^{5–8} They are also discussed as support-modifying functional layers in heterogeneous catalysis.^{9,10} For the successful transfer into application, it would be highly desirable to understand the processes at the IL|solid and IL|vacuum interface on a fundamental level, at the molecular scale. As one important point, this includes the various aspects of structure formation of ILs on flat surfaces, as a model for the IL|solid interface.

In this paper we report results of a combined experimental and theoretical study on the adsorption and structure formation behavior of the anion–cation pair 1-butyl-1-methylpyrrolidinium bis(trifluoromethylsulfonyl)imide, [BMP][TFSA], on Ag(111) under

* Address correspondence to juergen.behm@uni-ulm.de.

Received for review May 24, 2013 and accepted August 14, 2013.

Published online August 14, 2013
10.1021/nn4026417

© 2013 American Chemical Society

ultrahigh vacuum (UHV) conditions in the submonolayer to monolayer range, applying high-resolution scanning tunneling microscopy (STM), X-ray photoelectron spectroscopy (XPS), and dispersion-corrected density functional theory (DFT-D) calculations.¹¹ Despite numerous investigations, conducted both *in situ*, in an electrochemical environment^{12–16} and *ex situ* under UHV conditions,^{9,10,17–27} studies on the interaction of IL monolayers with single-crystalline surfaces are rare. Cremer *et al.* studied the adsorption of 1,3-dimethylimidazolium bis(trifluoromethylsulfonyl)imide ([MMIM][TFSA]) and 1-methyl-3-octylimidazolium bis(trifluoromethylsulfonyl)imide ([OMIM][TFSA]) ionic liquids on Au(111) by angle-resolved X-ray photoelectron spectroscopy (ARXPS) and concluded that at a coverage of up to 1.0 ML both anions and cations are in direct contact with the surface, presumably in an alternating arrangement.²⁸ (Note that the authors of that study defined a coverage of 1 ML as a saturated layer of anions and cations on top of each other, while in the present study we define a monolayer coverage by using the number of adsorbed ions in direct contact with the surface at saturation of the surface as reference. This requires multiplying the coverages from the above group by a factor of 2, which is done in the following.) In contrast to the findings for Au(111), Cremer *et al.* found for [MMIM][TFSA] adsorption on Ni(111) that up to coverages of \sim 0.80 ML the ions are vertically aligned, with the imidazolium cation directly on the Ni surface and the corresponding anion on top of it.²⁶ By analyzing infrared reflection absorption spectroscopy (IRAS) measurements with the help of density functional theory (DFT) calculations, Sobota *et al.* concluded that at submonolayer coverages the adsorption geometry of an imidazolium-based IL on Al₂O₃/NiAl(110) is likely to be a *cis*-conformation for [TFSA][–] anions, with the SO₂ groups attached to the substrate.²⁹

In a very first molecular resolution STM investigation, a short-range-ordered structure was resolved for the 1-butyl-1-methylpyrrolidinium tris(pentafluoroethyl)-trifluorophosphate ([BMP][FAP]) ionic liquid on Au(111) under UHV conditions at 200 K.³⁰ Molecular objects in the form of dots could be identified, which could be either ion pairs in a double-layer arrangement or individual ions, with both ions in contact with the surface. More recently, STM measurements by Foulston *et al.*³¹ on 1-ethyl-3-methylimidazolium bis(trifluoromethylsulfonyl)imide ([EMIM][TFSA]) adsorbed on Au(110) resolved molecular entities, which they assumed to consist of closely associated ion pairs. However, in neither of these cases was it possible to distinguish and to molecularly identify anions and cations by STM imaging. This is in contrast to other 2D ionic networks involving adsorbed alkali ions (Cs⁺, Na⁺, or Li⁺) and organic anions such as anionic carboxylate or tetracyano-*p*-quinodimethane adsorbed on smooth noble

metal surfaces (Cu(100), Au(111)),^{32–34} where STM identification of the respective adsorbed ions was possible in several cases. The relative size difference for the adsorbed IL species, however, is much less, rendering the identification of anions and cations much more complicated. In this context it is also of pivotal importance to obtain information on the actual ratio of adsorbed anions and cations on the surface. For a detailed molecular scale understanding of the processes at the IL|solid interface, the identification of single adsorbed ions would be highly desirable, together with a similar understanding of the nature of the substrate–adsorbate and adsorbate–adsorbate interactions. This is the topic of the present work, where the combination of high-resolution STM imaging with submolecular resolution, XPS measurements, and density functional theory-based calculations allows for an unambiguous identification of the different adsorbed species and gives detailed insight into the bonding situation of the adlayer, including both substrate–adsorbate and adsorbate–adsorbate interactions. To the best of our knowledge, this is the first time that individual ions could be resolved and identified in an IL adlayer, which is a prerequisite for the detailed understanding of the solid|IL interface in general. The latter in turn is the basis for systematic improvements in related applications as described above.

RESULTS AND DISCUSSION

To begin with, we discuss the adsorption behavior of [BMP][TFSA] on Ag(111) based on large-scale STM images at submonolayer and monolayer coverages. STM images recorded at 300 K do not allow us to resolve single IL entities. Instead, stripy features appear, which are not observed on the clean Ag(111) surface (SI I). Therefore these features are related to adsorbed IL entities in a 2D gas/2D liquid adlayer that diffuse rapidly on the time scale of the STM experiment and can therefore not be resolved.^{50–52} Similar observations were reported by Waldmann *et al.* for room-temperature imaging of a [BMP][FAP] ionic liquid adlayer on Au(111)³⁰ and by Foulston *et al.* for [EMIM][TFSA] on Au(110).³¹

In Figure 1 we present constant-current STM images recorded at submonolayer (Figure 1a) and monolayer coverage (Figure 1b) at around 100 K, where a monolayer is defined as the coverage required to completely cover the surface. Figure 1a shows four silver terraces (depicted as I, II, III, IV), which are covered with the adsorbed IL species in different ways. On terrace I, we find a large, long-range ordered and homogeneous adsorbate phase without any internal domain boundaries. These large ordered areas are solely observed on large silver terraces; small domains or islands of that phase, separated by domain boundaries or other phases, have not been observed on these terraces.

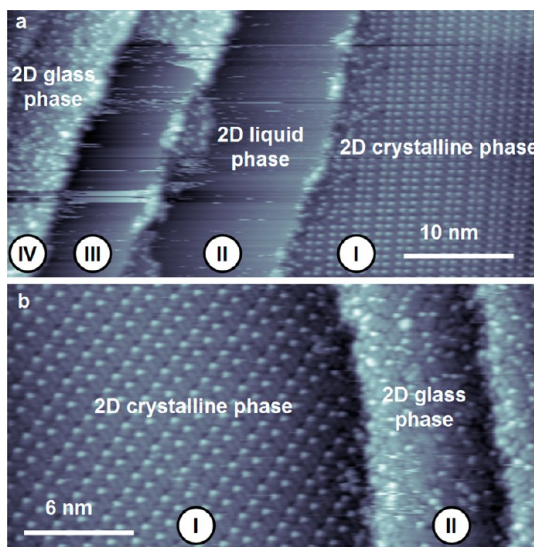


Figure 1. Constant-current STM images of [BMP][TFSA] on Ag(111) recorded at ~ 100 K. (a) The STM image at sub-monolayer coverage shows four silver terraces (indicated by numbers). Both an ordered 2D crystalline phase on the large Ag terrace and a disordered 2D glass phase on small Ag terraces (width ~ 10 nm) could be resolved. (b) At monolayer coverage, the large terrace is occupied by the ordered 2D crystalline, while small terraces are covered by the disordered 2D glass phase ((a) $U_t = -0.42$ V, $I_t = 110$ pA, (b) $U_t = -0.37$ V, $I_t = 130$ pA).

(We here consider terraces to be large, if they exhibit a width of at least 20–30 nm, and they extend mostly over the entire scan area in the other direction, which from experimental reasons was limited to 100 nm \times 100 nm.) These areas, which shall be referred to as an ordered 2D crystalline phase, mostly extend over the entire terrace, from step to step (see also SI II), while phase boundaries to an adjacent 2D liquid or 2D gas phase were largely orthogonal to the steps. From the reasons given above it was mostly not possible to determine the lengths of these areas, as they exceeded at least in one direction the STM scan area. Note that at large terraces, at least close to the steps, we also observed regions where the IL adsorbates are arranged in a disordered way, which will henceforth be referred to as a 2D glass phase. Terrace II (Figure 1a), which is only ~ 10 nm wide, shows an apparently uncovered, adsorbate-free region; at least there is no adlayer structure visible, neither ordered nor disordered. Noisy features in the fast scanning direction are again attributed to highly mobile adsorbed species; that is, also this area is not free of adsorbates. At the left side of terrace II, two islands with arbitrary shapes grow from the step. At the present resolution, these islands consist of single dots, which are arranged in a disordered way (see below). Terrace III (Figure 1a) shows a larger region covered with a disordered 2D glass phase, which extends from the left to the right step. Finally, terrace IV (Figure 1 a) is nearly completely filled with the disordered 2D glass phase.

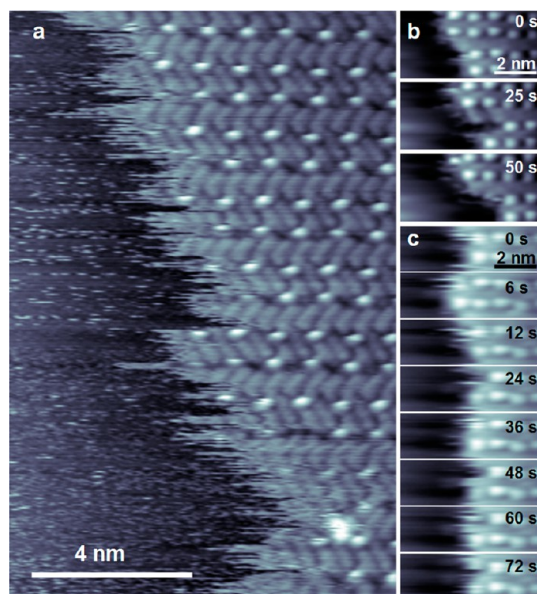


Figure 2. Constant-current STM images of [BMP][TFSA] on Ag(111) recorded at ~ 100 K. (a) STM image of the ordered 2D crystalline phase exhibiting frizzy features at the phase boundary to the 2D liquid phase, which are presumably due to exchange of adsorbed IL species at the phase boundary between 2D solid and 2D liquid. Time sequences of STM images with an image to image time of ~ 25 s in (b) and of ~ 6 s in (c) illustrate the dynamic changes at the phase boundary ((a) $U_t = -0.33$ V, $I_t = 150$ pA), (b) $U_t = -1.2$ V, $I_t = 90$ pA, (c) $U_t = -1.2$ V, $I_t = 100$ pA).

Successively increasing the coverage (Figure 1b), the 2D crystalline phase is exclusively found on the large terraces; in addition, also disordered regions are found on large terraces close to the steps. Narrow terraces (~ 10 nm width) in Figure 1b are now completely filled with the disordered 2D glass phase. As the influence of the steps is much larger at narrow terraces, it is likely that the interaction with these defects is responsible for the formation of the disordered 2D glass phase, inhibiting the ordering process. In large-scale STM images, three orientations of the 2D crystalline phase are found (only one orientation per terrace (SI II)), whose orientation differs by multiples of 120° . Hence, these domains are rotationally aligned with the underlying Ag(111) surface lattice. The observation that large terraces are largely occupied by large and homogeneous areas of 2D crystalline phase points toward (weakly) attractive adsorbate–adsorbate interactions.

Next we concentrate on the dynamic behavior of [BMP][TFSA] on Ag(111) at 100 K. Figure 2 shows the boundary between an ordered 2D crystalline phase and an adjacent 2D liquid phase, which typically appears frizzy (Figure 2a). Such frizzy features are generally due to surface mobility at the phase boundary. Even though we used a high tunneling resistance ($R_t \approx 2$ – 44 G Ω), we cannot totally exclude tip-induced effects. Time sequences of STM images were acquired, and selected images from two series are shown in Figure 2b and c. The time interval from image to image

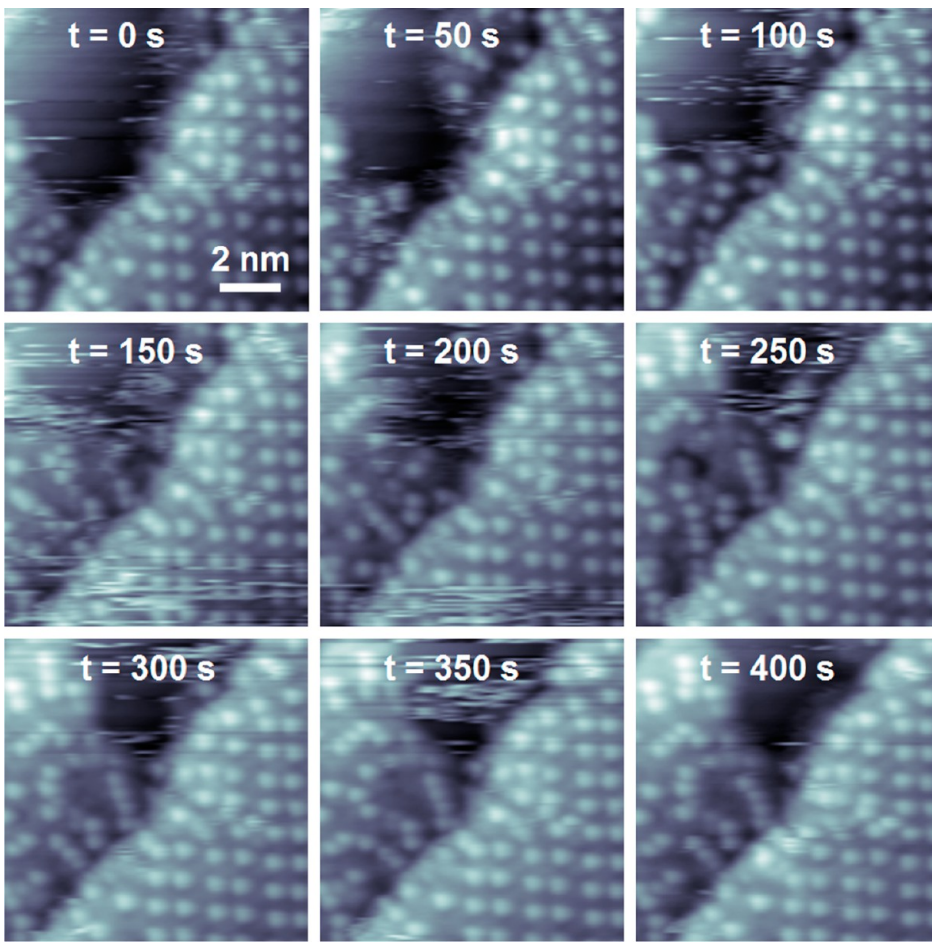


Figure 3. STM time sequence of [BMP][TFSA] on Ag(111) recorded at ~ 100 K. On the left Ag terrace, the phase boundary between disordered 2D glass and 2D liquid is monitored with a time interval from image to image of ~ 12 s (every fourth image is shown). Both the stripy features close to the phase boundary and the gradually changing phase boundary illustrate the exchange of adsorbed IL species between the phases. The right terrace is partly covered by a stable 2D crystalline phase ($U_t = -0.86$ V, $I_t = 50$ pA).

was ~ 25 s in Figure 2a and ~ 6 s in Figure 2b. The main finding is that the interior of the domain remains stable over time, while the location of the phase boundary changes gradually. This behavior can be explained by a 2D adsorption–desorption equilibrium at the phase boundary. The IL entities in the 2D liquid phase are highly mobile and cannot be resolved.^{50–52}

Dynamic STM measurements were also performed at regions of the surface where both the ordered 2D crystalline phase and the disordered 2D glass phase coexisted. Selected images extracted from the time lapse movie (see SI III) are shown in Figure 3. On the right terrace, the features in the ordered 2D crystalline phase remain highly stable over time. As in Figure 1a, disordered regions are found close to the step. On the left terrace, the STM time sequence shows that an apparently uncovered region successively fills up with IL species in the disordered 2D phase; that is, the phase boundary changes with time. As discussed before, the stripy features in the fast scan direction are presumably due to highly mobile adsorbed IL species in a 2D liquid phase.^{50–52} Thus, there is an exchange of adspecies at

the boundary between disordered 2D phase and 2D liquid. In contrast to the 2D crystalline phase, the adsorbed species in the disordered 2D phase are not fully immobile; infrequent molecular jumps are observed. Although we do not have experimental evidence for that, such molecular motion would allow, at least from a kinetic point of view, a slow transformation from the 2D disordered phase into the 2D crystalline phase. We assume, however, that both the interaction with the steps and the absence of strongly attractive adsorbate–adsorbate interactions prevent the adlayer from ordering on small terraces or directly along the steps on larger terraces. As described before, even at low temperatures of around 100 K we did not observe small islands of the ordered [BMP][TFSA] adlayer phase on Ag(111), but just larger ordered areas.

In similar time-resolved measurements we could resolve the 2D melting of the 2D crystalline phase. The results were acquired by applying “slow” linear heating ramps (~ 0.5 K/min), starting from an initial temperature of around 100 K. This way, we could reproducibly determine a 2D melting temperature of

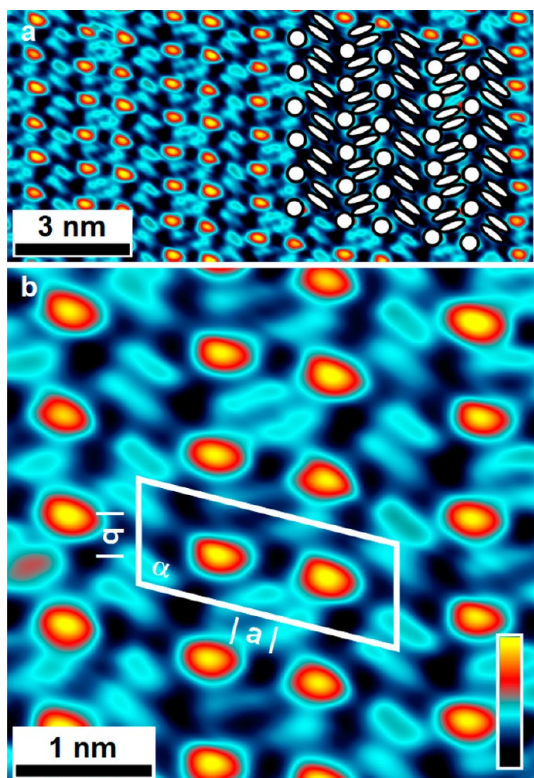


Figure 4. High-resolution STM images of [BMP][TFSA] on Ag(111) recorded at ~ 100 K. (a) High-resolution STM image of the ordered 2D crystalline phase; on the right-hand side dots and longish protrusions are superimposed on the image. (b) Enlarged STM image highlighting the structure of the ordered 2D crystalline phase. The unit cell is included ($|a| = 2.3 \pm 0.1$ nm, $|b| = 1.1 \pm 0.1$ nm, $\alpha = 98^\circ \pm 5^\circ$), which contains two dots and four longish protrusions ($U_t = -1.32$ V, $I_t = 110$ pA).

the ordered 2D crystalline phase of 180 ± 10 K. Above 180 K, we observed stripy features, which are attributed to a 2D liquid adlayer (SI IV). The “melting” temperature of the 2D glass phase is presumably slightly lower than that of the 2D crystalline phase; an accurate value cannot be given. However, extrapolating the intrinsic motion in this phase at 100 K to higher temperatures, a lower melting point compared to the ordered 2D crystalline phase seems plausible. In a more general sense, the presence of long-range ordered islands with a low melting point and their equilibrium with a surrounding 2D liquid phase point to weakly attractive adsorbate–adsorbate interactions and a low barrier for surface diffusion.

We now focus on the structure of the stable, ordered 2D crystalline phase. The high-resolution STM image of this phase in Figure 4a resolves an alternating sequence of pairs of longish protrusions and round dots, where the latter are indicated by symbols in the STM image. The dimensions of the unit cell are $|a| = 2.3 \pm 0.1$ nm, $|b| = 1.1 \pm 0.1$ nm, and $\alpha = 98 \pm 5^\circ$, with two dots and four longish protrusions per unit cell. Hence, the ratio of dots to longish protrusions is 1:2 (Figure 4b). The pairs of longish protrusions as well as

the dots are aligned along one of the lattice vectors, with always one line of dots followed by one line of longish protrusions. Between successive lines of longish protrusion their orientation changes by $\sim 120^\circ$. This together with the observation of three rotational domains indicates that the adlayer is aligned along the atomic lattice of the Ag(111) surface, most likely with the lines oriented along the close-packed directions of the Ag(111) surface.

To directly identify the ratio and composition of the adsorbed ions on the metal, in addition to the structural information gained by STM, XPS data were acquired on a Ag(111) surface covered by a submonolayer of [BMP][TFSA] at room temperature (from the damping of the Ag 3d signals a layer thickness of 3.5 Å was calculated). The C 1s and N 1s core level signals, which are common elements of both ions, are depicted in Figure 5a and b. A molecular stick presentation for [BMP][TFSA] is placed above the spectra; the color-coded arrows refer to the corresponding XPS peaks. In the C 1s region (Figure 5a), the peak referred to as C_{alkyl} originates from five carbon atoms, *i.e.*, three carbon atoms in the butyl chain and two carbon atoms in the pyrrolidinium ring, which both have solely carbon neighbors. The peak referred to as C_{hetero} is due to the four carbon atoms with the nitrogen atom in the ring as a neighbor, and C_{anion} is attributed to the two carbons in the anion; the nominal ratio of these peak areas is 5:4:2. The experimentally determined peak areas are 5.0:4.1:1.9 (normalized to C_{alkyl}), which is close to the nominal IL stoichiometry, indicating a 1:1 ratio of adsorbed anions and cations on the metal surface. In the N 1s region (Figure 5b), a $N_{\text{anion}}:N_{\text{cation}}$ ratio of 1 is found within the limits of accuracy, which further proves that the anion:cation ratio on the surface is 1:1. Overall, the XPS data provide clear proof that anions and cations adsorb without decomposition. Furthermore, upon successively increasing the [BMP][TFSA] coverage (Figure 5c), it was found that for small amounts of the IL on the surface the peak positions of the signals remain at constant binding energies, while for thicker films a gradual shift of all signals toward higher binding energies occurs, which reveals, in agreement with previous observations by Cremer *et al.* for [MMIM][TFSA] and [OMIM][TFSA] on Au(111),²⁸ that below 1 ML both anions and cations are directly adsorbed on the Ag surface, while at higher coverages condensed multilayer species dominate the spectra increasingly. (The peak shift is highlighted by the dashed lines in Figure 5c, which mark the positions of the fitted peaks for the submonolayer signal and for the 17.5 Å thick layer, respectively.)

Despite the detailed structural information gained from the STM data, it is not possible to identify the origin of the different features from these images alone. Further insight comes from DFT-D calculations, which provide a detailed understanding of the

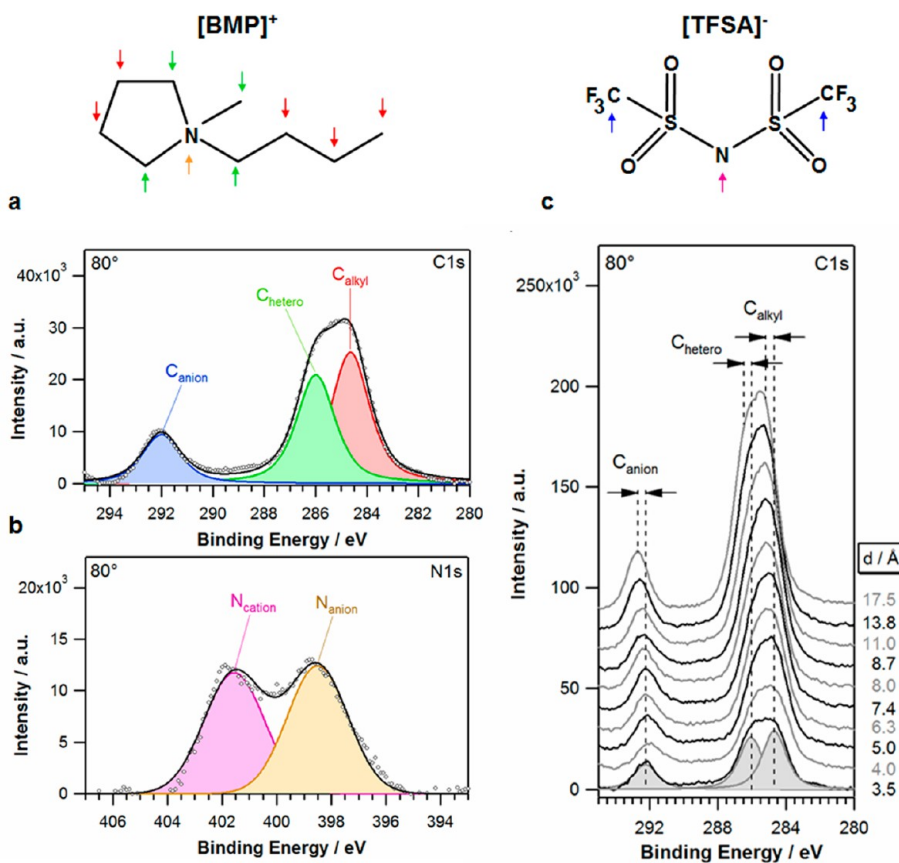


Figure 5. XP C 1s (a) and N 1s (b) core level spectra of a submonolayer [BMP][TFSA] layer on Ag(111) at room temperature (nominal thickness $\sim 3.5 \text{ \AA}$; see text). Stick presentations of the molecules are placed above the spectra. The color-coded arrows refer to the correspondingly color-coded XP peaks. The experimental peak areas are close to the nominal stoichiometry of the molecules, indicating that anions and cations are adsorbed on the surface with a ratio of 1:1. (c) Sequence of C 1s spectra for increasing coverage of [BMP][TFSA] on Ag(111). Dashed lines indicate the binding energies of the anion and cation related peaks in the limits of small coverages (adsorbed species with metal–adsorbate bond) and of high coverages (17.5 \AA film), reflecting condensed ion species (no metal–ion bond).

anion–cation adsorption complex and can explain the appearance in STM images for the given tunneling conditions. However, both the cation and the anion have many possible conformations at the surface due to rotation around the C–C, N–C, or S–C single bonds. In order to reduce the number of possible starting conformations of the adsorption structure of the IL pair, we will first analyze the most stable conformations of the isolated cation and the isolated anion. Especially for the cation, the orientation of the alkyl chain may have a strong impact on the appearance in the STM image and/or the packing density of the molecules at the surface. In the gas phase, the five-membered ring of [BMP]⁺ adopts an envelope conformation in which the butyl group occupies either the axial position (as shown in Figure 6a) or the equatorial position; that is, the butyl group is either perpendicular or parallel to the cyclopentane ring. For the isolated cation, the equatorial position is about 18 meV more stable. As this energetic difference is rather small and the actual conformation at the surface may depend on the coverage, the conformer with the butyl group in the axial position was considered as well. On the other hand,

it should also be considered that the axial position, with the butyl group sticking up when the imidazole ring is parallel to the surface, would allow a higher packing density.

To identify the most probable locations for the attachment of an anion, we evaluated the electrostatic potential at an isosurface of the total charge density of the [BMP]⁺ cation (see Figure 5a). The blue regions reveal the most positive electrostatic potential experienced by a positive test charge; that is, they indicate the regions where a negative (partial) charge would attach preferentially. In contrast, the red regions reveal the least positive electrostatic potential a positive test charge would experience. Accordingly, the anion most probably attaches in the middle of the triangle formed by the hydrogen atoms of the α -C atoms.

For the isolated [TFSA]⁻ anion, two stable conformations are obtained. In the first one, the CF_3 groups are both located above (or below) the S–N–S plane, which is subsequently denoted as *cis*-conformation. In the second conformation, which is accordingly termed as *trans*-conformation, one CF_3 group is above and the other one below the S–N–S plane. The *trans*-conformer

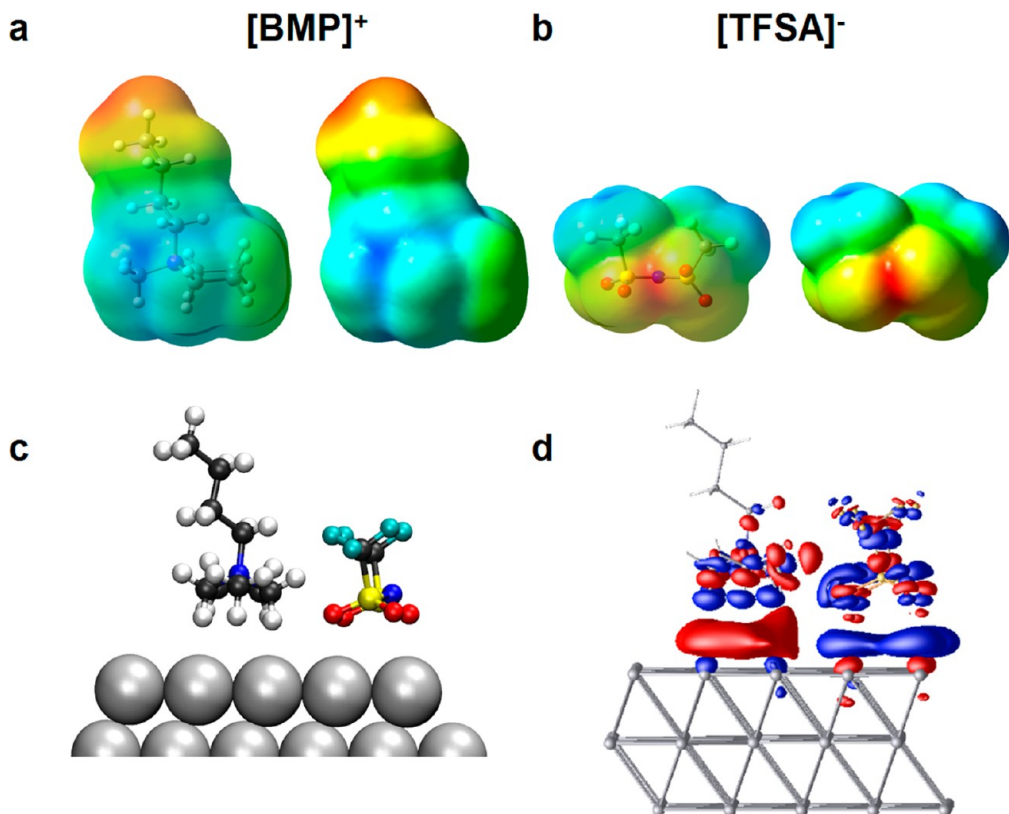


Figure 6. Electrostatic potential at an electron charge isosurface (isosurface charge density $4 \times 10^{-4} \text{ e/bohr}^3$) of (a) $[\text{BMP}]^+$ (view onto the $\text{C}_{\text{butyl}}-\text{N}-\text{C}_{\text{methyl}}$ plane) and (b) $[\text{TFSA}]^-$ (view along the $\text{S}-\text{N}-\text{S}$ plane). Red regions refer to the least positive/most negative electrostatic potential a positive test charge experiences. Blue regions reveal the most positive/least negative electrostatic potential a positive test charge experiences. (c) Side view of the adsorption complex of the ionic liquid ion pair on $\text{Ag}(111)$. (d) Isosurfaces ($-0.0058 \text{ e/}\text{\AA}^3$ (blue) and $+0.0049 \text{ e/}\text{\AA}^3$ (red)) of the adsorption-induced changes in the charge density of $[\text{BMP}][\text{TFSA}]$ adsorbed on $\text{Ag}(111)$. The chosen values for the isosurfaces depict a total electron shift of 0.205e from the blue regions into the red regions.

is about 40 meV more stable than the *cis*-conformer. Additionally, the rotational barrier that needs to be overcome for transferring from one into the other conformer is rather small, in the range of 50–100 meV. Sobota *et al.* reported for an imidazolium-based ionic liquid that in the multilayer both the *cis*- and the *trans*-conformers of $[\text{TFSA}]^-$ coexist, whereas in the monolayer the *cis*-conformer is found on a $\text{Al}_2\text{O}_3/\text{NiAl}(110)$ support.²⁹ Considering the adsorbed ionic liquid rather than an individual anion, two additional factors may affect the relative stability of the respective conformers: the interaction with the counterion, here the cation, and the interaction with the surface. Due to these interactions, even quite different conformers might be involved in the most stable complexes. Similar to the procedure for the $[\text{BMP}]^+$ cation, the electrostatic potential is calculated at and mapped onto an isosurface of the total charge density of the $[\text{TFSA}]^-$ anion (see Figure 5b) to estimate possible positions of attached cations. For both the *cis*- and the *trans*-conformation (not shown), the most attractive regions for positive charges (red regions) are within the $\text{S}-\text{N}-\text{S}$ plane. In order to probe the possible changes in the stability induced by an attached cation,

we choose the alkali metal ion Li^+ as a simple model. Both the *cis*- and the *trans*-conformers of $[\text{TFSA}]^-$ lead to stable complex structures with the alkali metal cation. Due to the similar stabilization of both $[\text{TFSA}]^-$ conformers upon interaction with the cation, the *trans*-conformer is more stable than the *cis*-conformer also in a cation–anion complex.

To elucidate effects resulting from the interaction with the substrate, we first explore the adsorption of $[\text{TFSA}]^-$ on $\text{Ag}(111)$. In that case, the *trans*-conformer leads to the most stable adsorption structure, being about 0.2 eV more stable than the metastable *cis*-conformer. Both the *cis*- and the *trans*-conformer adsorb with their respective dipole moment aligned normal to the surface, with the negatively charged end of the molecule oriented toward the surface. The adsorption distances of both conformers are comparable as well. The distance between the average z -position of the O atoms (only two atoms are taken into account in the case of the *trans*-conformer) and the Ag atoms of the topmost surface layer is 2.472 and 2.717 Å for the *trans*- and *cis*-conformer, respectively.

Although we have worked out stable anion and cation conformations in the gas phase and at the

surface, there are still many possibilities for the structure at the surface. In the following we restrict the discussion to only one possibility that has been found to be theoretically stable and that is compatible with our experimental results. A valuable experimental input is that the appearance and the size of the unit cell of [BMP][TFSA] on Ag(111) and others that we observed for related ILs with different alkyl groups ([EMIM][TFSA], [OMIM][TFSA]) are nearly identical, which is a strong indication that the alkyl chain of the cation adopts the axial position, pointing toward the vacuum. Furthermore, the XPS data (Figure 5) clearly indicated that both the cation and the anion are in contact with the surface. Similar findings were also reported for ARXPS measurements for the adsorption of [MMIM][TFSA] on Au(111).²⁸ The authors of the latter study also proposed that the oxygen atoms of adsorbed $[\text{TFSA}]^-$ are pointing toward the surface, whereas the fluoromethyl groups are directed toward the vacuum. These experimental findings suggest that the butyl group of adsorbed $[\text{BMP}]^+$ adopts the axial position and the *cis*-conformer of adsorbed $[\text{TFSA}]^-$ is present in the monolayer of [BMP][TFSA] on Ag(111). Although, as shown above, both this conformation itself and its adsorption are less stable than that of the *trans*-conformer, it might still lead to a more stable structure of the total adsorption complex due to more favorable adsorbate–adsorbate interactions, as the electrostatic potential of $[\text{TFSA}]^-$ is most negative in the S–N–S plane, which in turn is parallel to the surface in the case of the *cis*-conformer. Thus, the interactions with neighboring cations are expected to be stronger than in the case of the *trans*-conformer where the S–N–S plane (and thus the most negative electrostatic potential) is normal to the surface.

When looking at the structure of the adsorption complex (see Figure 6c) and comparing it to that of pure adsorbed $[\text{TFSA}]^-$ (in the *cis*-conformation), there are barely any differences: the anion is only slightly further away from the surface (about 0.10 Å) than for the pure adsorbed $[\text{TFSA}]^-$. The adsorption energy with respect to the ionic liquid pair in the gas phase is 1.30 eV. However, 95% of the adsorption energy is due to dispersion interactions; that is, all other interactions (electrostatic interactions, covalent bonding) lead to an adsorption energy of only 0.06 eV. The charge density difference map (Figure 6d) provides an insight into the electronic changes occurring upon adsorption. Upon adsorption, electrons are shifted from the blue regions to the red regions. As expected, there is a depletion of electron charge in the region between the anion and the surface, whereas it is enhanced in the region between the surface and the cation. Thus, the ion pair induces a lateral dipole at the surface that is opposite in sign to the dipole generated by the two adsorbed ions. For the understanding of the adsorption bond it would be interesting to know whether the

enhanced/depleted electron density is due to a charge transfer from the surface to the ionic liquid (and *vice versa*) or whether it is due to polarization effects within the individual components. This could tell us whether the charge remains at the ionic liquid or whether there is a significant charge transfer to/from the adsorbed species. In the first case, there will be considerable electrostatic adsorbate–adsorbate interactions, which lead to the formation of an ordered structure. In the second case, ordering has to occur *via* different mechanisms, *e.g.*, weaker dipolar interactions or van der Waals interactions between adsorbates, and indirect (surface-mediated) adsorbate–adsorbate interactions. However, it is hard to distinguish between charge transfer and polarization effects, as the assignment of charges to individual components mainly depends on the position of the border between them. Therefore, different methods for charge analysis that are based on different dividing schemes can lead to very diverse results. In order to get at least a rough estimate of the charge distribution within the system, we used the Bader charge analysis. We found that the charges of the cation and the anion hardly change upon adsorption on Ag(111). This is in agreement with the rather small interaction energy of 0.06 eV if dispersive interactions are excluded, *i.e.*, with the absence of any significant covalent bond formation.

In Figure 7a we show simulated STM images of two possible adsorption structures with comparable adsorption energy. These simulations suggest that the experimentally observed dots in the high-resolution STM images correspond to the cations. This seems to be the only way to explain the large corrugation of the isosurface of the partial electronic density contributing to the STM image. The longish protrusions could be related to the adsorbed anion. It seems that each anion leads to two longish protrusions, each of them stemming from 2 F atoms of the fluoromethyl groups. This could explain the ratio of 1:2 of dots to longish protrusions. Furthermore, different voltages in between –0.3 and –1.5 V have been studied; however, no voltage dependency could be observed.

Following the STM simulations, the anion–cation pairs in the ordered 2D crystalline phase are depicted in the high-resolution STM image in Figure 7b on the right-hand side by superimposed dots and longish protrusions. To allow for a direct comparison with the simulated STM images, we inserted a pseudo-three-dimensional STM representation with a similar scale to that used in the simulated presentation in the left lower corner of Figure 7b. Apparently, the IL structure is formed by an alternating sequence of rows in which the anion–cation pairs exhibit the same azimuthal orientation. In this herringbone-type arrangement, the azimuthal orientation of the ion pairs changes by 120° between subsequent rows. The unit cell is included as well; it contains two dots and four longish

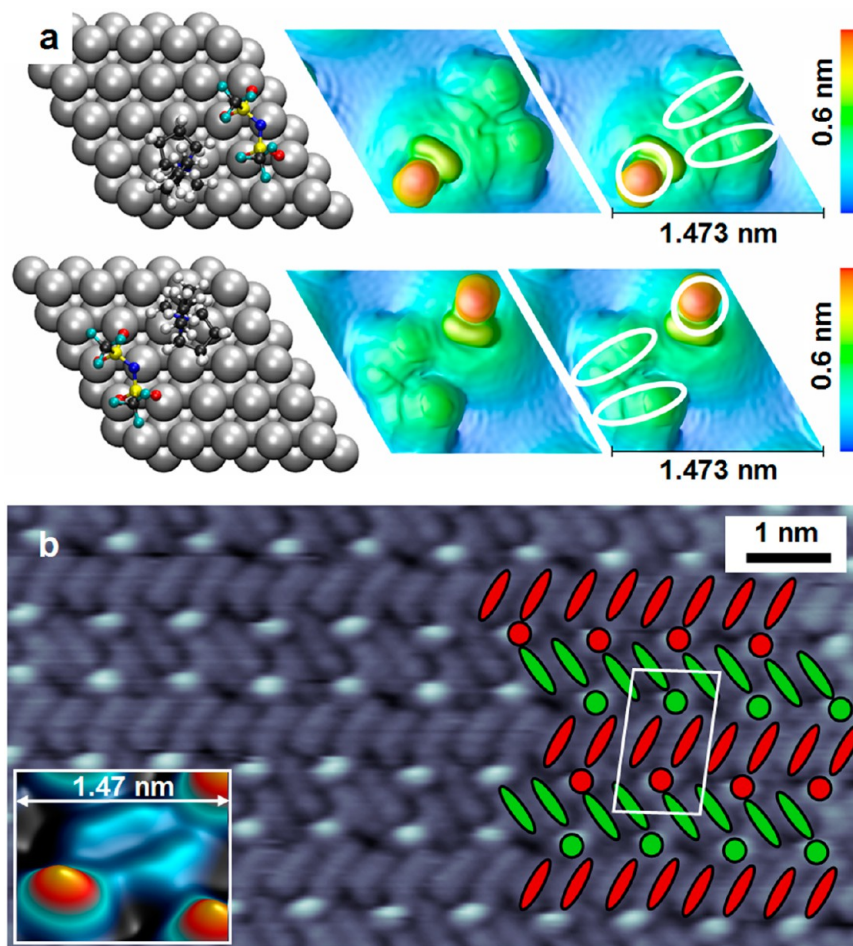


Figure 7. (a) Ball-and-stick presentation of two mirror symmetric configurations of the adsorbed IL ions together with the corresponding simulated STM images ($U_t = -1.35$ V, isosurface value = 3×10^{-7} e/Å³) of the adsorption structures of [BMP][TFSA] on Ag(111). The dots and longish protrusions seen in the experimental STM images are indicated on the right. (b) High-resolution STM image of the ordered 2D solid phase. On the right-hand side, the anion and cations are labeled by schematic drawings, and the unit cell is marked ($U_t = -0.33$ V, $I_t = 150$ pA). The inset in the left lower corner shows a pseudo-three-dimensional STM representation with a magnified scale, exhibiting the scale as that in the simulated image.

protrusions, which are now identified as two “anion–cation pairs” with different orientations. It should be noted that the term “adsorbed ion pair” is insofar misleading as we have no indication for a structure dominated by strongly attractive interactions between intact ion pairs and weak interactions between neighboring ion pairs. Instead, Figure 7b clearly demonstrates that the spacing between anions and cations is rather similar, resembling a 2D ion crystal. Furthermore, the layer is rotationally aligned with the substrate, possibly due to the interaction of the oxygen atoms of the anion with the surface.

Finally it should be noted that for computational reasons the DFT calculations discussed so far were performed for a simplified unit cell with a (5×5) geometry with quasi-isolated adsorbed ion pairs (one ion pair per unit cell) (see section 2.2), while the unit cell depicted in Figure 4b containing two ion pairs is equivalent to a (4×9) periodicity. However, we also performed a structure optimization within the correct (4×9) periodicity with two ion pairs per unit cell (see

Supporting Information SI V), starting with the configuration of the isolated ion pairs. Because of the large computational costs for these calculations, due to the large number of variable parameters for relaxing the adlayer structure, we had to reduce the thickness of the Ag slab to one layer so that the STM simulations cannot be reliably based on this calculation. Yet, we obtained only a slight structural rearrangement leading to a stabilization by ~0.3 eV in a shallow minimum. This indicates that the adlayer is rather flexible and that there are only relatively weak interactions between the adsorbates. Considering the small variation in energetics and electronic structure, this also means that the STM simulations obtained within the (5×5) cells can be used to interpret the observed structural elements. These findings also mean that further optimization of the adlayer is likely to not have a strong impact on the energetics (substrate–adsorbate and adsorbate–adsorbate interactions). This latter finding is in good agreement with expectations for an adlayer system dominated by repulsive interactions.

CONCLUSIONS

Having investigated the interaction of [BMP][TFSA] with Ag(111) and the structure formation in the adlayer by variable-temperature STM measurements and DFT-based calculations, we arrive at the following results and conclusions:

1. Following deposition of [BMP][TFSA] on Ag(111) at room temperature and cool-down to around 100 K, we observed the coexistence of an ordered 2D crystalline phase, a disordered 2D glass phase, and a 2D liquid phase. The 2D glass phase was solely observed on small Ag(111) terraces ($d \approx 10$ nm) and is probably induced by the interaction with the steps and the lateral confinement. On large Ag(111) terraces, long-range ordered and homogeneous domains are formed without any internal domain boundaries.
2. Variable-temperature STM measurements reveal melting of the ordered 2D crystalline phase at 180 ± 10 K.
3. Dynamic STM measurements at around 100 K resolve exchange of adspecies at the phase boundaries 2D crystalline phase|2D liquid and disordered 2D glass|2D liquid. While the interior of the ordered 2D crystalline phase is stable over time, infrequent molecular jumps are observed in the 2D glass phase.
4. The fact that we observe long-range ordered domains with a low 2D melting point and an equilibrium between the 2D crystalline phase and the 2D liquid phase points to weakly

attractive adsorbate–adsorbate interactions and a low surface diffusion barrier.

5. Room-temperature XPS measurements confirm adsorption of the [BMP] cation and the [TFSA] anion with an anion:cation ratio of 1:1, where both ions are in direct contact with the metal surface. Furthermore, they show that IL species adsorb intact, without decomposition.
6. DFT-D calculations reveal a stable adsorption complex for one IL pair with the anion and the cation laterally placed side by side. The butyl group of the cation points toward the vacuum, and the anion exhibits a *cis*-conformation of the S–N–S plane, with the SO₂ groups binding to the surface and the trifluoromethyl groups pointing toward the interface IL|vacuum. STM simulations agree with the molecular features in high-resolution STM images, allowing us to identify anions and cations. In addition, the calculations show that the charge remains at the ionic liquid and the interaction with the substrate mainly occurs almost exclusively *via* dispersion interactions and weak electrostatic (dipole–induced dipole) interactions. The ordered 2D crystalline phase is stabilized by weakly attractive electrostatic interactions between the positive and negative charges of the adsorbed ions. Finally, the layer is rotationally aligned with the substrate surface, probably due to the interaction of the oxygen atoms of the anion with the surface.

METHODS

Experimental Methods. The STM experiments were performed in a two-chamber UHV system, at a background pressure in the low 10^{-10} mbar regime. The microscope is an Aarhus type STM (SPECs Aarhus STM 150), which allows measuring at variable temperatures between 100 and 400 K by cooling with liquid nitrogen and resistive heating. The tunneling current was between 20 and 150 pA, and the applied bias voltage between -0.1 and -1.5 V referred to the sample. The images were recorded in constant-current mode. Variable-temperature STM experiments were conducted with a heating rate of ~ 0.5 K/min. The Ag(111) single crystal was purchased from MaTeck; the ionic liquid [BMP][TFSA], from Merck in ultrapure quality. Clean Ag(111) surfaces were prepared by Ar⁺-ion sputtering (500 eV) and annealing to 770 K. Prior to deposition on Ag(111), [BMP][TFSA] was degassed in UHV for at least 24 h in a previously baked out crucible. The ionic liquid was evaporated onto the Ag substrate held at room temperature with a commercial Knudsen effusion cell for organic molecules (Ventiotec, OVD-3), which was heated to 373 K. The evaporation rates were previously checked by a quartz microbalance. The sample was cooled to a temperature of roughly 100 K in a time span of 2–3 h before the STM measurements.

The XPS experiments were performed in a different UHV system, equipped with a SPECs spectrometer, an Al K α X-ray source (1486.6 eV) operated at a power of 250 W ($U = 14$ kV, $I = 17.8$ mA), and a hemispherical energy analyzer (DLSEGD-Phoibos-Has3500). Spectra were recorded at a pass energy of 100 eV. The photoelectrons were detected at an emission angle

(θ) of 80° relative to the surface normal to increase the surface sensitivity. The adsorbate layer thickness d was calculated by analysis of the damping of the substrate Ag 3d levels according to $I_d = I_0 \exp(-d/\lambda \cos \theta)$, with λ being the inelastic mean free path, which was calculated by Tanuma *et al.* to be ~ 3.3 nm at kinetic energies of 1100 eV.³⁵ Before analysis of the spectra, a Shirley background was subtracted from all C 1s signals; in the N 1s region this was done by a polygon baseline. In the peak fitting procedure, a Voigt-type peak shape was applied, which was approximated by a weighted sum of Gaussian and Lorentzian functions.

Calculational Methods. Periodic DFT calculations were performed using the exchange–correlation functional of Perdew, Burke, and Ernzerhof (PBE)³⁶ as implemented in the Vienna *ab initio* simulation package (VASP).^{37,38} In order to account for dispersive interactions missing in the exchange–correlation functionals of the generalized gradient approximation (GGA), we employed Grimme's correction scheme of 2010 (DFT-D3).¹¹ It has recently been shown that this approach yields reliable adsorption energies and structures for organic molecules and hydrogen-bonded networks on metal surfaces.^{39–41} Ion cores are represented by means of the projector augmented wave (PAW) method.^{42,43} The electronic one-particle wave functions were expanded in a plane wave basis set up to an energy cutoff of 400 eV.

The Ag(111) surface was represented by a slab consisting of three metal layers, separated by a vacuum region of about 25 Å. To model the adsorption of one cation–anion pair at the surface, we chose a Ag(111)-(5×5) overlayer structure with one adsorbed cation–anion pair per unit cell. For the integration

over the first Brillouin zone a $2 \times 2 \times 1$ Monkhorst–Pack k-point mesh⁴⁴ with a Methfessel–Paxton smearing of 0.1 eV was employed. The geometry of the adsorption complex was optimized by relaxing all atoms of the IL pair and the atoms of the uppermost layer of the metal surface. Only these atoms were taken into account for the evaluation of dispersive interactions.

STM simulations are based on the Tersoff–Hamann approximation.⁴⁵ Within that model the tunneling current is proportional to the local density of states (LDOS) at the surface close to the Fermi energy at the position of the tip. Constant-current images are simulated by an isosurface of the LDOS integrated between the Fermi energy of the system and the sample bias.

Isolated molecules have also been calculated using the GAUSSIAN09 code⁴⁶ in connection with the atom-centered basis set aug-cc-pVTZ.^{47–49} For isolated molecules no dispersion corrections have been employed.

Conflict of Interest: The authors declare no competing financial interest.

Acknowledgment. B.U. gratefully acknowledges a fellowship by the Fonds der Chemischen Industrie.

Supporting Information Available: STM image at 300 K showing a highly mobile 2D liquid adlayer; large-scale STM images including different rotational domains; time lapse movie showing the 2D crystalline and the 2D glass phase; variable-temperature STM images; (9 \times 4) unit cell used for the simulation of the STM images. This material is available free of charge via the Internet at <http://pubs.acs.org>.

REFERENCES AND NOTES

1. Welton, T. Room-Temperature Ionic Liquids. Solvents for Synthesis and Catalysis. *Chem. Rev.* **1999**, *99*, 2071–2084.
2. *Ionic Liquids in Synthesis*, 2nd ed.; Wasserscheid, P., Welton, T., Eds.; Wiley-VCH: New York, 2008.
3. Wasserscheid, P.; Keim, W. Ionic Liquids—New “Solutions” for Transition Metal Catalysis. *Angew. Chem., Int. Ed.* **2000**, *39*, 3772–3789.
4. Plechko, N. V.; Seddon, K. R. Applications of Ionic Liquids in the Chemical Industry. *Chem. Soc. Rev.* **2008**, *37*, 123–150.
5. Kuboki, T.; Okuyama, T.; Ohsaki, T.; Takami, N. Lithium-Air Batteries Using Hydrophobic Room Temperature Ionic Liquid Electrolyte. *J. Power Sources* **2005**, *146*, 766–769.
6. Armand, M.; Tarascon, J.-M. Building Better Batteries. *Nature* **2008**, *451*, 652–657.
7. Armand, M.; Endres, F.; MacFarlane, D. R.; Ohno, H.; Scrosati, B. Ionic-Liquid Materials for the Electrochemical Challenges of the Future. *Nat. Mater.* **2009**, *8*, 621–629.
8. Girishkumar, G.; McCloskey, B.; Luntz, A. C.; Swanson, S.; Wilcke, W. Lithium-Air Battery: Promise and Challenges. *J. Phys. Chem. Lett.* **2010**, *1*, 2193–2203.
9. Steinrück, H.-P.; Libuda, J.; Wasserscheid, P.; Cremer, T.; Kolbeck, C.; Laurin, M.; Maier, F.; Sobota, M.; Schulz, P. S.; Stark, M. Surface Science and Model Catalysis with Ionic Liquid-Modified Materials. *Adv. Mater.* **2011**, *23*, 2571–2587.
10. Steinrück, H.-P. Recent Developments in the Study of Ionic Liquid Interfaces Using X-ray Photoelectron Spectroscopy and Potential Future Directions. *Phys. Chem. Chem. Phys.* **2012**, *14*, 5010–5029.
11. Grimmel, S.; Antony, J.; Ehrlich, S.; Krieg, H. A Consistent and Accurate *ab Initio* Parametrization of Density Functional Dispersion Correction (DFT-D) for the 94 Elements H–Pu. *J. Chem. Phys.* **2010**, *132*, 154104–154119.
12. Atkin, R.; El Abedin, S. Z.; Hayes, R.; Gasparotto, L. H. S.; Borisenko, N.; Endres, F. AFM and STM Studies on the Surface Interaction of [BMP]TFSA and [EMIm]TFSA Ionic Liquids with Au(111). *J. Phys. Chem. C* **2009**, *113*, 13266–13272.
13. Endres, F.; Höft, O.; Borisenko, N.; Gasparotto, L. H. S.; Prowald, A.; Al Salman, R.; Carstens, T.; Atkin, R.; Bund, A.; El Abedin, S. Z. Do Solvation Layers of Ionic Liquids Influence Electrochemical Reactions? *Phys. Chem. Chem. Phys.* **2010**, *12*, 1724–1732.
14. Atkin, R.; Borisenko, N.; Drüschler, M.; El Abedin, S. Z.; Endres, F.; Hayes, R.; Huber, B.; Roling, B. An *in Situ* STM/AFM and Impedance Spectroscopy Study of the Extremely Pure 1-Butyl-1-methylpyrrolidinium Tris(pentafluoroethyl)-trifluorophosphate/Au(111) Interface: Potential Dependent Solvation Layers and the Herringbone Reconstruction. *Phys. Chem. Chem. Phys.* **2011**, *13*, 6849–6857.
15. Drüschler, M.; Borisenko, N.; Wallauer, J.; Winter, C.; Huber, B.; Endres, F.; Roling, B. New Insights into the Interface between a Single-Crystalline Metal Electrode and an Extremely Pure Ionic Liquid: Slow Interfacial Processes and the Influence of Temperature on Interfacial Dynamics. *Phys. Chem. Chem. Phys.* **2012**, *14*, 5090–5099.
16. Gnahn, M.; Berger, C.; Arkhipova, M.; Kunkel, H.; Pajkossy, T.; Maas, G.; Kolb, D. M. The Interfaces of Au(111) and Au(100) in a Hexaalkyl-Substituted Guanidinium Ionic Liquid: An Electrochemical and *in Situ* STM Study. *Phys. Chem. Chem. Phys.* **2012**, *14*, 10647–10652.
17. Smith, E. F.; Rutten, F. J. M.; Villar-Gracia, I. J.; Briggs, D.; Licence, P. Ionic Liquids in Vacuo: Analysis of Liquid Surfaces Using Ultra-High-Vacuum Techniques. *Langmuir* **2006**, *22*, 9386–9392.
18. Höft, O.; Bahr, S.; Himmerlich, M.; Krischok, S.; Schaefer, J. A.; Kemper, V. Electronic Structure of the Surface of the Ionic Liquid [EMIM][Tf₂N] Studied by Metastable Impact Electron Spectroscopy (MIES), UPS, and XPS. *Langmuir* **2006**, *22*, 7120–7123.
19. Maier, F.; Gottfried, J. M.; Rossa, J.; Gerhard, D.; Schulz, P. S.; Schwieger, W.; Wasserscheid, P.; Steinrück, H.-P. Surface Enrichment and Depletion Effects of Ions Dissolved in an Ionic Liquid: An X-Ray Photoelectron Spectroscopy Study. *Angew. Chem., Int. Ed.* **2006**, *45*, 7778–7780.
20. Armstrong, J. P.; Hurst, C.; Jones, R. G.; Licence, P.; Lovelock, K. R. J.; Satterley, C. J.; Villar-Garcia, I. J. Vapourisation of Ionic Liquids. *Phys. Chem. Chem. Phys.* **2007**, *9*, 982–990.
21. Souda, R. Glass-Liquid Transition, Crystallization, and Melting of a Room Temperature Ionic Liquid: Thin Films of 1-Ethyl-3-methylimidazolium Bis[trifluoromethanesulfonyl]imide Studied with TOF-SIMS. *J. Phys. Chem. B* **2008**, *112*, 15349–15354.
22. Deyko, A.; Lovelockqq, K. R. J.; Corfield, J. A.; Taylor, A. W.; Gooden, P. N.; Villar-Garcia, I. J.; Licence, P.; Jones, R. G.; Krasovskiy, V. G.; Chernikova, E. A.; et al. Measuring and Predicting $\Delta_{\text{vap}}H_{298}$ Values of Ionic Liquids. *Phys. Chem. Chem. Phys.* **2009**, *11*, 8544–8555.
23. Lovelockqq, K. R. J.; Villar-Garcia, I. J.; Maier, F.; Steinrück, H. P.; Licence, P. Photoelectron Spectroscopy of Ionic Liquid-Based Interfaces. *Chem. Rev.* **2010**, *110*, 5158–5190.
24. Sobota, M.; Schmid, M.; Happel, M.; Amende, M.; Maier, F.; Steinrück, H.-P.; Paape, N.; Wasserscheid, P.; Laurin, M.; Gottfried, J. M.; et al. Ionic Liquid Based Model Catalysis: Interaction of [BMIM][Tf₂N] with Pd Nanoparticles Supported on an Ordered Alumina Film. *Phys. Chem. Chem. Phys.* **2010**, *12*, 10610–10621.
25. Maier, F.; Cremer, T.; Kolbeck, C.; Lovelockqq, K. R. J.; Paape, N.; Schulz, P. S.; Wasserscheid, P.; Steinrück, H. P. Insights into the Surface Composition and Enrichment Effects of Ionic Liquids and Ionic Liquid Mixtures. *Phys. Chem. Chem. Phys.* **2010**, *12*, 1905–1915.
26. Cremer, T.; Wibmer, L.; Calderon, S. K.; Deyko, A.; Maier, F.; Steinrück, H.-P. Interfaces of Ionic Liquids and Transition Metal Surfaces—Adsorption, Growth, and Thermal Reactions of Ultrathin [C₁C₁Im][Tf₂N] Films on Metallic and Oxidised Ni(111) Surfaces. *Phys. Chem. Chem. Phys.* **2012**, *14*, 5153–5163.
27. Schernich, S.; Laurin, M.; Lykhach, Y.; Steinrück, H.-P.; Tsud, N.; Skala, T.; Prince, K. C.; Taccardi, N.; Matolin, V.; Wasserscheid, P.; et al. Functionalization of Oxide Surfaces through Reaction with 1,3-Dialkylimidazolium Ionic Liquids. *J. Phys. Chem. Lett.* **2012**, *4*, 30–35.
28. Cremer, T.; Stark, M.; Deyko, A.; Steinrück, H.-P.; Maier, F. Liquid/Solid Interface of Ultrathin Ionic Liquid Films: [C₁C₁Im][Tf₂N] and [C₈C₁Im][Tf₂N] on Au(111). *Langmuir* **2011**, *27*, 3662–3671.

29. Sobota, M.; Nikiforidis, I.; Hieringer, W.; Paape, N.; Happel, M.; Steinrück, H.-P.; Görling, A.; Wasserscheid, P.; Laurin, M.; Libuda, J. Toward Ionic-Liquid-Based Model Catalysis: Growth, Orientation, Conformation, and Interaction Mechanism of the $[\text{Tf}_2\text{N}]$ Anion in $[\text{BMIM}][\text{Tf}_2\text{N}]$ Thin Films on a Well-Ordered Alumina Surface. *Langmuir* **2010**, *26*, 7199–7207.

30. Waldmann, T.; Huang, H.-H.; Hoster, H. E.; Höft, O.; Endres, F.; Behm, R. J. Imaging an Ionic Liquid Adlayer by Scanning Tunneling Microscopy at the Solid | Vacuum Interface. *ChemPhysChem* **2011**, *12*, 2565–2567.

31. Foulston, R.; Gangopadhyay, S.; Chiutu, C.; Moriarty, P.; Jones, R. G. Mono- and Multi-Layer Adsorption of an Ionic Liquid on $\text{Au}(110)$. *Phys. Chem. Chem. Phys.* **2012**, *14*, 6054–6066.

32. Stepanow, S.; Ohmann, R.; Leroy, F.; Lin, N.; Strunkus, T.; Wöll, C.; Kern, K. Rational Design of Two-Dimensional Nanoscale Networks by Electrostatic Interactions at Surfaces. *ACS Nano* **2010**, *4*, 1813–1820.

33. Skomski, D.; Abb, S.; Tait, S. L. Robust Surface Nano-Architecture by Alkali-carboxylate Ionic Bonding. *J. Am. Chem. Soc.* **2012**, *134*, 14165–14171.

34. Wäckerlin, C.; Iacovita, C.; Chylareka, D.; Fesser, P.; Jung, T. A.; Ballav, N. Assembly of 2D Ionic Layers by Reaction of Alkali Halides with the Organic Electrophile 7,7,8,8-Tetracyano-p-quinodimethane (TCNQ). *Chem. Commun.* **2011**, *47*, 9146–9148.

35. Tanuma, S.; Powell, C. J.; Penn, D. R. Calculations of Electron Inelastic Mean Free Paths. Data for 14 Organic Compounds over the 50–2000 eV Range. *Surf. Interface Anal.* **1993**, *21*, 165–176.

36. Perdew, J. P.; Burke, K.; Ernzerhof, M. Generalized Gradient Approximation Made Simple. *Phys. Rev. Lett.* **1996**, *77*, 3865–3868.

37. Kresse, G.; Furthmüller, J. Efficiency of *ab Initio* Total Energy Calculations for Metals and Semiconductors Using a Plane-Wave Basis Set. *Comput. Mater. Sci.* **1996**, *6*, 15–50.

38. Kresse, G.; Furthmüller, J. Efficient Iterative Schemes for *ab Initio* Total-Energy Calculations Using a Plane-Wave Basis Set. *Phys. Rev. B* **1996**, *54*, 11169–11186.

39. Tonigold, K.; Groß, A. Adsorption of Small Aromatic Molecules on the (111) Surfaces of Noble Metals: A Density Functional Theory Study with Semiempirical Corrections for Dispersion Effects. *J. Chem. Phys.* **2010**, *132*, 224701–224701–10.

40. Tonigold, K.; Groß, A. Dispersive Interactions in Water Bilayers at Metallic Surfaces: A Comparison of the PBE and RPBE Functional Including Semiempirical Dispersion Corrections. *J. Comput. Chem.* **2012**, *33*, 695–701.

41. Waldmann, T.; Nenon, C.; Tonigold, K.; Hoster, H. E.; Groß, A.; Behm, R. J. The Role of Surface Defects on Large Organic Molecule Adsorption: Substrate Configuration Effects. *Phys. Chem. Chem. Phys.* **2012**, *14*, 10726–10731.

42. Blöchl, P. E. Projector Augmented-Wave Method. *Phys. Rev. B* **1994**, *50*, 17953–17979.

43. Kresse, G.; Joubert, D. From Ultrasoft Pseudopotentials to the Projector Augmented-Wave Method. *Phys. Rev. B* **1999**, *59*, 1758–1775.

44. Monkhorst, H. J.; Pack, J. D. Special Points for Brillouin-Zone Integrations. *Phys. Rev. B* **1976**, *13*, 5188–5192.

45. Tersoff, J.; Hamann, D. R. Theory of the Scanning Tunneling Microscope. *Phys. Rev. B* **1985**, *31*, 805–813.

46. Frisch, M. J.; Trucks, G. W.; Schlegel, H. B.; Scuseria, G. E.; Robb, M. A.; Cheeseman, J. R.; Scalmani, G.; Barone, V.; Mennucci, B.; Petersson, G. A.; et al. *Gaussian 09*, Revision B.01; Gaussian, Inc.: Wallingford, CT, 2010.

47. Dunning, T. H., Jr. Gaussian Basis Sets for Use in Correlated Molecular Calculations. I. The Atoms Boron through Neon and Hydrogen. *J. Chem. Phys.* **1989**, *90*, 1007–1023.

48. Kendall, R. A.; Dunning, J.; Harrison, R. J. Electron Affinities of the First-Row Atoms Revisited. Systematic Basis Sets and Wave Functions. *J. Chem. Phys.* **1992**, *96*, 6796–6806.

49. Woon, D. E.; Dunning, J. Gaussian Basis Sets for Use in Correlated Molecular Calculations. III. The Atoms Aluminum through Argon. *J. Chem. Phys.* **1993**, *98*, 1358–1371.

50. Yanagi, H.; Mukai, H.; Ikuta, K.; Shibutani, T.; Kamikado, T.; Yokoyama, S.; Mashiko, S. Molecularly Resolved Dynamics for Two-Dimensional Nucleation of Supramolecular Assembly. *Nano Lett.* **2002**, *2*, 601–604.

51. Berner, S.; de Wild, M.; Ramoino, L.; Ivan, S.; Baratoff, A.; Güntherodt, H. J.; Suzuki, H.; Schlettwein, D.; Jung, T. A. Adsorption and Two-Dimensional Phases of a Large Polar Molecule: Sub-Phthalocyanine on $\text{Ag}(111)$. *Phys. Rev. B* **2003**, *68*, 115410.

52. Buchner, F.; Zillner, E.; Röckert, M.; Gläsel, S.; Steinrück, H.-P.; Marbach, H. Substrate-Mediated Phase Separation of Two Porphyrin Derivates on $\text{Cu}(111)$. *Chem. Eur. J.* **2011**, *17*, 10266–10229.